Momentum considerations on the New MEXICO experiment

E A Parra[1,2], K Boorsma[3], J G Schepers[3] and H Snel[3]

[1] Royal Institute of Technology (KTH), Stockholm, Sweden
[2] Aristotle University of Thessaloniki (AUTH), Thessaloniki, Greece
[3] Energy research Centre of the Netherlands (ECN), Petten, The Netherlands

E-mail: eapb@kth.se, boorsma@ecn.nl

Abstract.

The present paper regards axial and angular momentum considerations combining detailed loads from pressure sensors and the flow field mapped with particle image velocimetry (PIV) techniques. For this end, the study implements important results leaning on experimental data from wind tunnel measurements of the New MEXICO project. The measurements, taken on a fully instrumented rotor, were carried out in the German Dutch Wind tunnel Organisation (DNW) testing the MEXICO rotor in the open section. The work revisits the so-called momentum theory, showing that the integral thrust and torque measured on the rotor correspond with an extent of 0.7 and 2.4% respectively to the momentum balance of the global flow field using the general momentum equations. Likewise, the sectional forces combined with the local induced velocities are found to plausibly obey the annular streamtube theory, albeit some limitations in the axial momentum become more apparent at high inductions after a=0.3. Finally, azimuth induced velocities are measured and compared to predictions from models of Glauert and Burton et al., showing close-matching forecasts for blade spans above 25%.

1. Introduction

The flow around wind turbines is governed by the conservation laws of fluid dynamics, namely mass, energy and momentum. These principles can be applied in combination with the inviscid and incompressible flow assumptions, which added to the representation of a rotor as an actuator disk, lead to the so-called actuator disk or momentum theory.

This theory is of common practical use in rotor aerodynamics (mainly with the BEM method), though it suffers from several limitations. Firstly, the representation of the rotor as an actuator disk, combined with the use of inviscid and incompressible flow properties, does not lead to simple analytic formulations. The number of unknowns would exceed the number of equations, so further assumptions and/or additional equations need to be introduced. The typical assumptions are known not to be rigorously valid (see e.g. [3]), but reduce the complexity of the general system of equations (the so-called general momentum theory [2]), enabling closed-form solutions in exchange of reduced fidelity. Consequently, a thorough examination of the validity of momentum methods is only possible with a comparative study. Examples for CFD cases can be found in [6] for actuator disks, whereas vortex methods vs BEM can be consulted in [7].

In this case, an experiment is used for the comparative analysis with a real rotor. The New MEXICO project is a good framework for such purpose given the extensive details measured [1]. It is worth mentioning that especially the enhanced PIV capabilities, in relation to the previous MEXICO project [8], make it suitable for undertaking a study combining loads and velocities.

2. Objectives

The present investigation is particularly focused on reconstructing a comprehensive axial and angular momentum balance for the MEXICO rotor using detailed load and flow field measurements from the New MEXICO experiment. By virtue of the experimental attributes not only the integral momentum balance of the global flow field can be achieved, but also an assessment of annular momentum is possible as well. Here, an advantage is taken from the fact that the experiment provides extensive details of the flow field, enabling the momentum considerations to be accomplished for a more complete, and not necessarily simplified scenario. This permits to compare the results with those of simpler complexity, deducing in turn the possible scope or limitations of the theory in axial flow conditions.

3. Experimental setup

The experiment features a three-bladed rotor of 4.5m diameter instrumented with 148 pressure taps recording at 5514 Hz and distributed over the 25%, 35%, 60%, 82% and 92% spanwise sections. The pressure field over the blades was integrated to determine the aerodynamic forces. The velocity field, on the other hand, was measured using stereo PIV techniques. The space domain mapped is depicted in Figures 1-2.

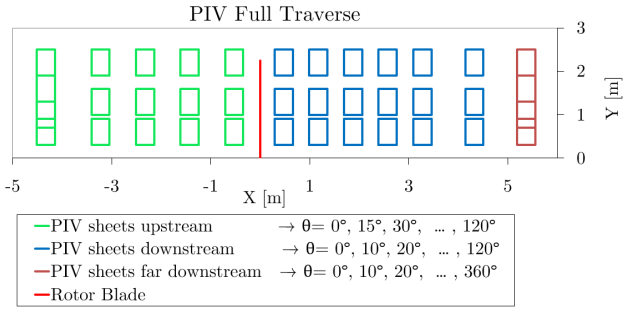

Figure 1. Full traverse

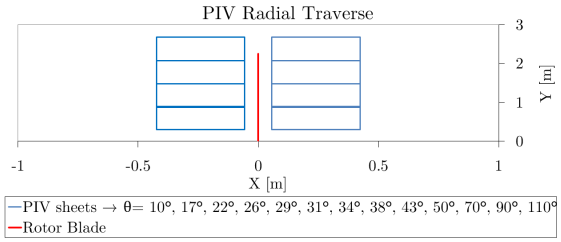

Figure 2. Radial traverse

Both PIV planar setups depicted above contemplate also swept azimuth positions as if they were revolved around the X axis (see the angles indicated in the legend under Figures 1 and 2). Thus they can be reckoned as cylindrical volume sections encompassing the rotor. The Full Traverse has been carried out at a tip speed ratio of $\lambda = 6.67$, whereas the Radial Traverse is available at $\lambda = 4.16$, 6.67 and 9.96.

In terms of accuracy, the PIV velocities have an approximate uncertainty within a range of 0.1 to 0.2 m/s. This was corroborated by perceiving flow discontinuities between some of the adjacent PIV sheets. The discontinuities are produced by a so-called peak locking effect, being it a systematic error inherent to digital PIV [4]. The effect of this inaccuracy was investigated verifying the conservation of mass flow using large control volumes. The conservation is nevertheless obeyed with a maximum error of 0.95% (0.1% for the actual CV used in the integral momentum analysis). The pressure sensors, on the other hand, have a maximum uncertainty of 35 Pa as estimated from [5]. This would make the inner sections exposed to lower dynamic pressures more susceptible to load fluctuations. This was appraised comparing cases with repeated conditions, finding a maximum deviation of 1.5% in sectional loads and torques.

Notable pressure fluctuations were found in some sensors at $\lambda = 4.16$, an uncertainty inherent to flow separation in some regions. The deviation of time averaged sectional loads between those compared cases is however less than 1%. This means that the flow unsteadiness is somehow counterbalanced by the high pressure readings that diminish the relative influence of the sensor accuracy, thus capturing almost the same load ranges on each run.

It ought to be mentioned that the sectional loads were calculated from chordwise integration assuming a linear pressure variation between adjoined sensors around the airfoils. The uncertainty associated to this reduced smoothness has not been assessed.

4. Momentum analysis in the global flow field

The Full Traverse configuration (Figure 1) is suitable for an integral control volume analysis owing to its large-size scale. In light of this, a balance of mass and momentum can be effectuated, being this later directly comparable with the integral forces on the rotor.

The general forms of axial and angular momentum balance for an arbitrary control volume in absence of transient and viscous terms read:

$$F_x = \int_A V_x \rho \mathbf{V} \cdot d\mathbf{A} + \int_A P d\mathbf{A} \qquad (1) \qquad\qquad Q = \int_A \rho r V_\theta \mathbf{V} \cdot d\mathbf{A} \qquad (2)$$

where F_x and Q are the axial force and torque, and $\mathbf{V}$ (V_x, V_r, V_θ) is the velocity vector in cylindrical coordinates. Momentum theory considers an axially-expanding control volume with constant mass flow (see Figure 3). In the classical theory, pressure force terms are neglected. This does not pose problems in Equation 2, but it is an intrinsic part of Equation 1. This surface force arises mainly from the pressure reduction in the slipstream due to wake rotation [9].

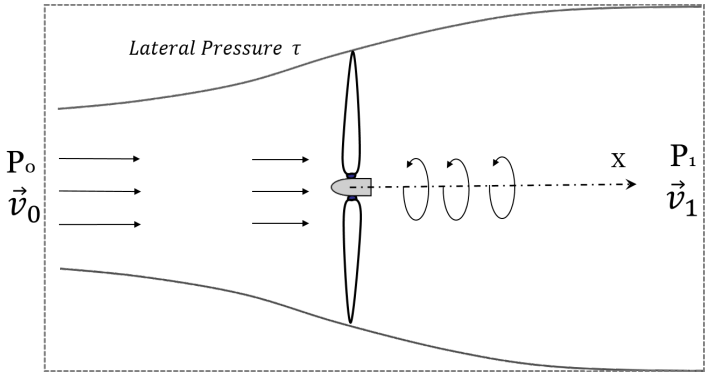

Figure 3. Expanding control volume with constant mass flow

Introducing the radial balance equation as:

$$\frac{dP}{dr} = \rho \frac{V_\theta^2}{r} \qquad (3)$$

The axial momentum can be transformed into:

$$\begin{aligned} F_x &= \int_A V_x \rho \mathbf{V} \cdot d\mathbf{A} + \int_{A_1} \left(\int_{r_1}^{R_1} \rho \frac{V_{\theta_1}^2}{r_1} dr_1 \right) dA_1 \\ &= \rho \int_{A_0} V_{x_0}^2 dA_0 - \rho \int_{A_{up}} V_{r_{up}} V_{x_{up}} dA_{up} - \rho \int_{A_1} V_{x_1}^2 dA_1 + \int_{A_1} \left(\int_{r_1}^{R_1} \rho \frac{V_{\theta_1}^2}{r_1} dr_1 \right) dA_1 \end{aligned} \qquad (4)$$

In this way, the integrals can be computed from the velocity field, whereas the left-hand-sides are obtained from the integrated blade pressures. The integrals were calculated here along the cylindrical boundaries of Figure 1 (in analogy to the outer squared area in Figure 3). The subscript *up* refers to the upper boundary enveloping the CV along x at the maximum radius. The results were found to differ by 2.34% in axial force and 0.1% in torque with respect to the expanding streamtube control volume.

The ultimate wake velocities in the equation above (see also Figure 3) need to be considered from a position sufficiently far behind the rotor such that the radial velocities tend to zero (no flow expansion), but not too far as otherwise mixing of the streamtube wake and the outer flow may occur. This was judged to be adequate at 5.4m downstream (see Figure 1), or equivalently 1.2 rotor diameters, where the zero radial velocity is satisfied with deviations in the order of ± 0.05 m/s and an average and maximum of $V_{r_{avg}} = 0.02$ and $V_{r_{max}} = 0.11$ m/s respectively. This location was also judged to be out of the zone of perturbations from wind tunnel effects based on a previous CFD study from DTU of the full wind tunnel geometry [13].

Numerical integration of the previous equations gives the global momentum forces. These forces can be made non-dimensional using the typical thrust and power coefficients:

$$C_T = \frac{F_x}{\frac{1}{2}\rho V_\infty^2 A_r} \qquad (5) \qquad\qquad C_p = \frac{Q \cdot \Omega}{\frac{1}{2}\rho V_\infty^3 A_r} \qquad (6)$$

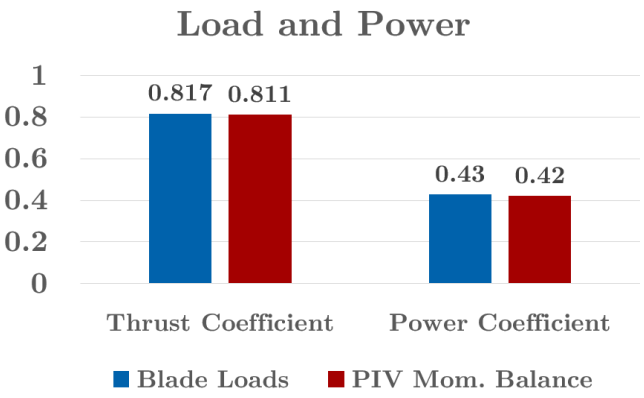

Figure 4. Integral load and power at λ=6.67. Blade loads vs. resultant momentum

A comparison of the momentum forces (red) with the the blade loads (blue) is shown in Figure 4. The blade loads have been reconstructed by integration of the sectional forces assuming linear variation between adjoined stations and zero loads at the root and the tip. This method was found to underpredict the axial force by approximately 5% based on CFD results. Therefore, C_T (from blades) has been compensated by this factor already in Figure 4. The torque was not altered due to the unknown, but opposed effect of viscous drag neglection on the pressure taps.

An agreement of 0.73% is found between both blade loads and PIV in the axial force. It is important to mention that the momentum term associated to the pressure deficit in the wake attains a 15% of the total force. This stresses the fact that both right-hand-side terms in Equation 1 are indeed complementary. That is, the radial ditribution of pressure in the wake has influence in the distribution of axial velocity as well.

For the power, a difference of 2.38% is found between the two approaches. These are somewhat expected since the pressure sensors neglect viscous forces. The number of sensors is reminded to be inevitably limited in chord and spanwise directions which may also lead to an offset in accuracy compared to the PIV-based results.

5. Momentum analysis in annular sections

An important feature of the BEM method is that the blade-element equations stand for sectional or differential forces, so in order to couple them with actuator disk theory, the integral momentum equations need to be applied in differential or annular sections (see Figure 5).

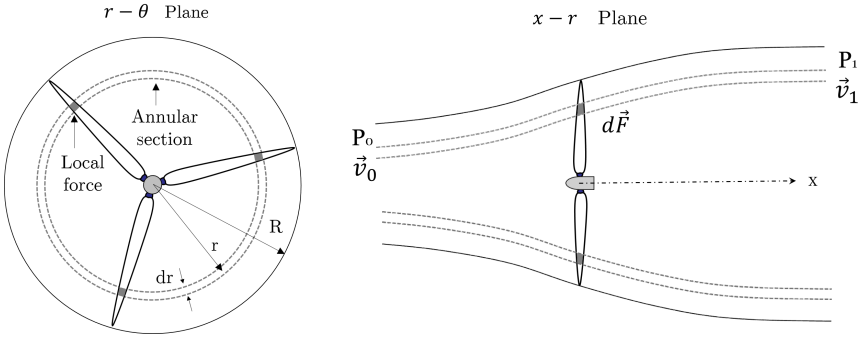

Figure 5. Annular streamtube

In the following, the axial and angular momentum considerations will be examined on the basis of this differential approach.

5.1. Axial momentum equations

Using a differential streamtube, the axial momentum translates from Equation 1 to the following form:

$$dF_x(r) = \underbrace{\rho V_x(V_{x_0} - V_{x_1})dA}_{\text{change in momentum}} + \underbrace{(P_0 - P_1)dA_1}_{\text{wake pressure deficit}} + \underbrace{\Delta X}_{\text{lateral pressure}} \tag{7}$$

where the force ΔX, produced by the lateral pressure surrounding the annular streamtube along X, is incorporated in the axial momentum balance [10]. In BEM, the two pressure terms from Equation 7 are disregarded, thus arriving to the well-known relation:

$$C_T(r) = 4a(1-a) \tag{8}$$

This is the usual form derived from the classical momentum theory without rotation. In this case, however, it is applied at radially independent sections instead of the full disk.

The validity of this approximation can be tested with respect to the experiment. The local force C_T is known at the five pressure stations over the blade, whereas the axial inductions is to be retrieved from the Radial Traverse of PIV (see Figure 2).

5.2. Axial induction from PIV

The determination of rotor induced velocities from PIV is not trivial. Considerations need to be made for:

- The azimuthal flow non-uniformity (caused by a finite no. of blades), see Figure 6.
- Interpolation in x at the rotor plane

For the first-mentioned, an azimuth average was verified with two approaches. One way to proceed is to do the average along the full θ blade range from $\theta_o = 0°$ to $\theta_f = 120°$, here recalled as the full azimuth average:

$$\overline{V_x} = \frac{1}{\theta_f - \theta_o} \int_{\theta_o}^{\theta_f} V_x(\theta) d\theta \tag{9}$$

A second approach is to exclude from the average calculation the up and down peak regions markedly influenced by the blade passage at 30° (see azimuth distribution in Figure 6). The azimuth angles removed in this situation are then $10° < \theta < 50°$. This later method, here recalled as reduced azimuth average, appears to be justified due to the seemingly *symmetry* of velocities around the blade. As can be observed in Figure 7, both approaches yield similar azimuth average results. This was verified to hold approximately true for most of the blade span at different wind speeds (see Figure 8). The zones where discrepancies may be found are those very close to the blade tip (r/R > 0.96), where the influence of the tip vortex gains relevance. It is possible that a similar behavior takes place at the root vortex. Nevertheless, missing data was found there for some azimuth positions, thus hindering a more detailed evaluation.

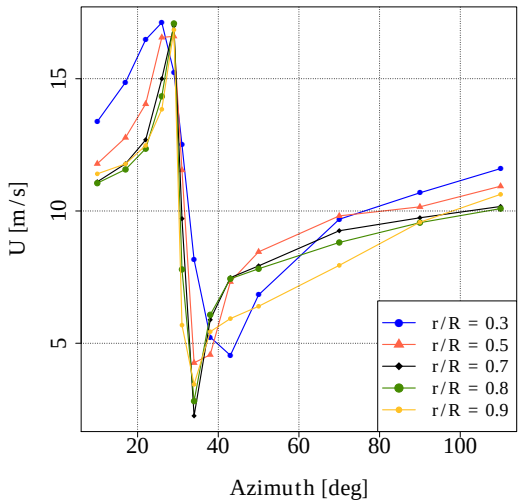

Figure 6. Azimuth distribution of axial velocity for several radial span positions at x=0.1m downstream

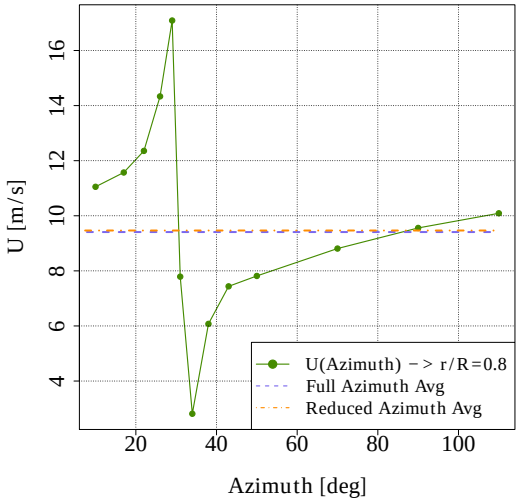

Figure 7. Azimuth distribution of axial velocity at r/R=0.8 and x=0.1m downstream. Comparison with the full and reduced azimuth average values

Another aspect appraised was the influence of the proximity of planes used for interpolation of velocity at the rotor surface. Several offset distances were employed and the velocity was non-dimesionalized using the definition of axial induction factor:

$$a = 1 - \frac{V_{x_{rotor}}}{V_{x_0}} \tag{10}$$

where $V_{x_{rotor}}$ is the estimated velocity at $x = 0$. The planes used for calculation of the axial induction are situated at $x = \pm 0.07, \pm 0.1, \pm 0.2, \pm 0.3$, and ± 0.4 meters from the blades. In addition to this, higher order methods were also utilized: bicubic interpolation and cubic spline fitting over all the x planes at each radial position, using the full sheets. The results are shown in Figures 10 - 12.

All the curves render approximately the same values as consequence of the close proximity between the PIV areas with the blade. Only care need to be taken for the tip regions at $\lambda = 9.96$ where rapid flow expansion takes place.

The later two interpolations, however, fail to predict the near-root values due to the amount of null data contained therein (see e.g. blank regions in Figure 16). Because of this, the rotor plane velocities have been retrieved considering a simple interpolation from a distance of ±0.1m

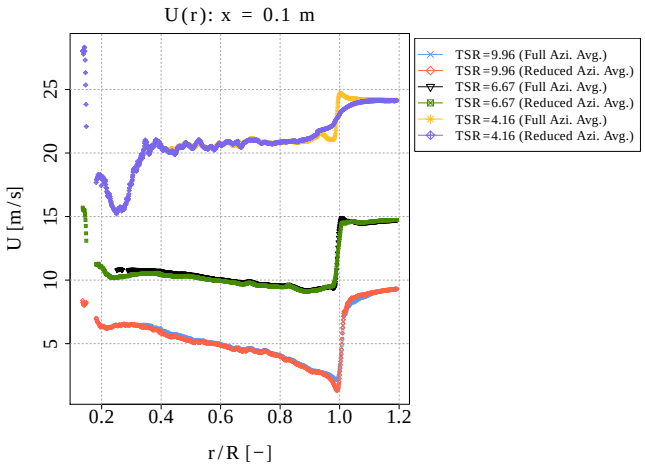

Figure 8. Comparison of azimuth average approaches for different tip speed ratios at x=0.1m downstream

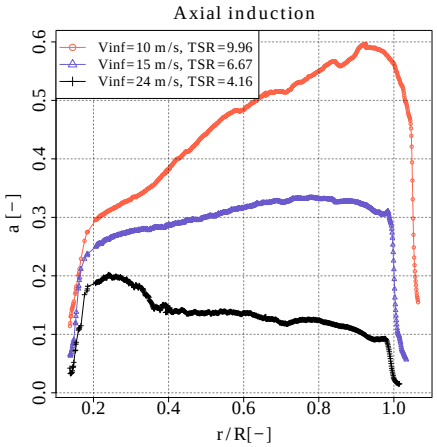

Figure 9. Non-dimensional radius vs. axial induction at three λ

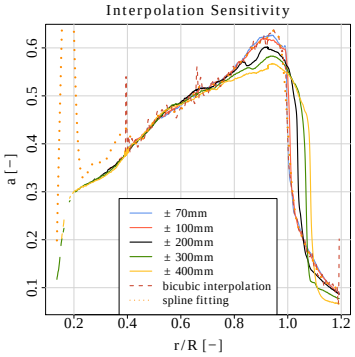

Figure 10. Interpolation sensitivity of $a(r)$ at $\lambda = 9.96$. Full azimuth average

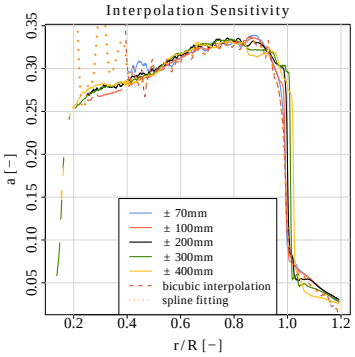

Figure 11. Interpolation sensitivity of $a(r)$ at $\lambda = 6.67$. Full azimuth average

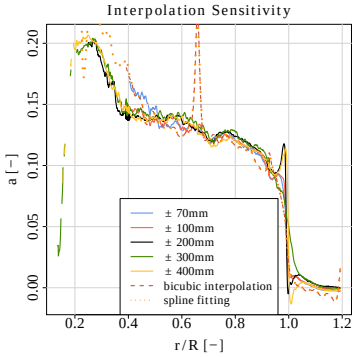

Figure 12. Interpolation sensitivity of $a(r)$ at $\lambda = 4.16$. Full azimuth average

from the blades, and a distance of ±0.23m whenever empty data is found at the inboard sections. It can be noticed, that changing from one plane of interpolation to another has little effect at inner radii. The differences are actually within the PIV uncertainty range (0.1 to 0.2m/s) and so this can be exploited without expecting a substantial loss of accuracy.

Contemplating the aforementioned factors, the rotor induction has been computed with a full azimuth average and with the interpolation planes previously described. The radial distribution is provided in Figure 9.

5.3. Assessment of axial momentum theory at the annulii

By creating data points from the local blade loads with the corresponding induced velocities at three tip speed ratios, a diagram can be constructed as shown in Figure 13. The solid line represents the theoretical momentum curve from Equation 8 and the empirical straight dotted line connects the momentum curve with the high loading states after $a = 0.35$ up to the turbulent wake state. The different colors in data points denote a different operating condition and the different characters denote a different radial position.

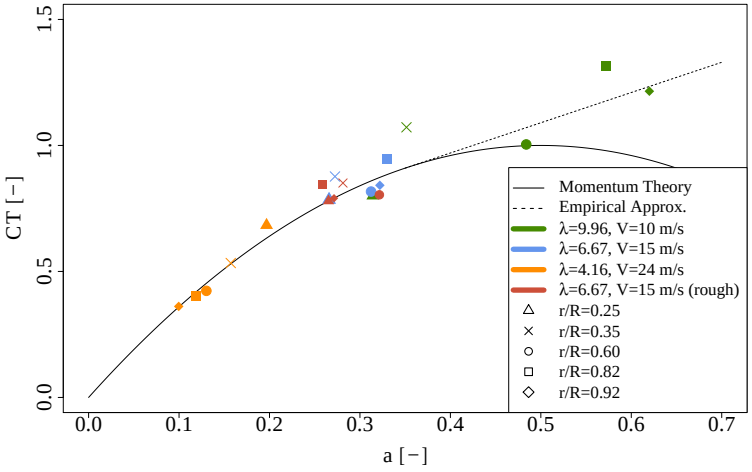

Figure 13. Thrust coefficient vs. axial induction. Comparison of the momentum curve with respect to the actual measured local force and induction.

Generally speaking, the momentum line plausibly follows a good trend with the experimental results. This confirms that the force associated to the change in momentum is very dominant indeed. It is to be noted that at lower inductions the data points remain very close to the theory. In contrast, the data points around $a = 0.3$ and higher scatter more notably around the momentum curve. Values in the turbulent wake near $a = 0.5$ and above are out of the theoretical scope and are quite dispersed accordingly.

Considering the difference between C_T values predicted by the momentum curve and the actual measurements, the mean absolute error (MAE) of the momentum theory is 5.6% for the data points below $a = 0.4$ (valid momentum region). The mean absolute error for data points situated between $0.25 < a < 0.4$ is 6.2%, and for data points below $a = 0.25$ (data points in orange) the MAE reduces to 3.9%. Overall, the spread increases with a; this suggests that the pressure forces neglected (second and third terms on the RHS of Equation 7) may become more relevant at high loading states.

At $\lambda = 6.67$ it is possible to check further theoretical assumptions. Assuming that $P_0 = P_1$, the simple actuator disk theory, derives that V_x at the rotor is half (or the average of) the free and slipstream axial velocities, that is:

$$V_{x_{rotor}} = \frac{V_{x_0} + V_{x_1}}{2} \quad \rightarrow \quad b = 2a \tag{11}$$

or in other words, the axial induction in the wake (denoted b) becomes twice as the rotor. BEM implicitly uses this approximation in annular streamtubes. Therefore, the flow can be traced from the rotor down to the ultimate wake using the Full Traverse at several radial positions to check the scope of this approximation. For this task the streamline paths were traced from the velocity vectors at $\lambda = 6.67$ (see Figure 14) in order to account for the flow expansion in the wake. The result of the axial inductions in the rotor ($2a$) and the far wake (b) are shown in Figure 15.

The curves get fairly close to each other, thus confirming the approximation quality of the mentioned assumption, at least for the blade span covered. It is nonetheless important to note that the tip and root regions are not involved here. This was due to constraints arising from the limited space domain mapped, combined with areas containing null or contaminated data.

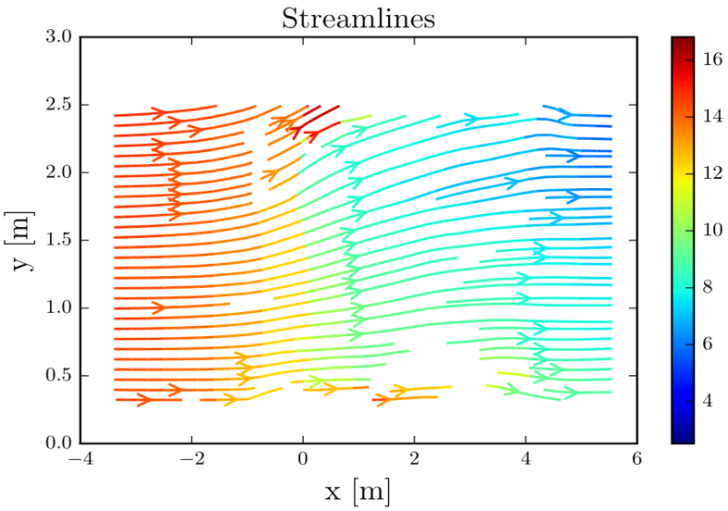

Figure 14. Velocity map in the full traverse, $\lambda = 6.67$. Color scale representing the axial velocity magnitude (in m/s).

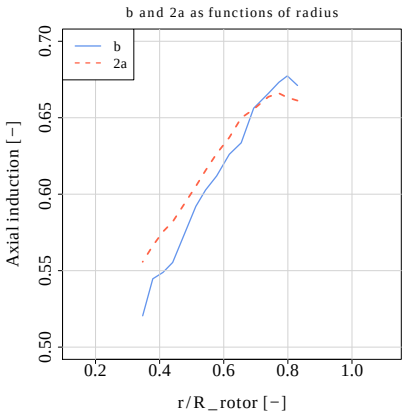

Figure 15. Comparison between the axial induction at the far wake and the rotor

5.4. Radial distribution of angular momentum

Unlike the axial case, the angular momentum does not suffer from limitations arising from neglected terms, nor corrections referred to the operating state of the turbine. Hence, the blade torque in BEM is only coupled to the angular momentum imparted to the wake. Since this reaction is also a function of the radius, the angular momentum for an annular streamtube (see Figure 5) in the near wake can be compared to the sectional torque on the blades as follows:

$$dQ(r) = \rho V_{x_w} r V_{\theta_w} dA_w \tag{12}$$

The subscript w denotes the wake location, here referred to closely behind the rotor. The circumferential velocities, however, are not uniformly developed therein as shown in Figure 16

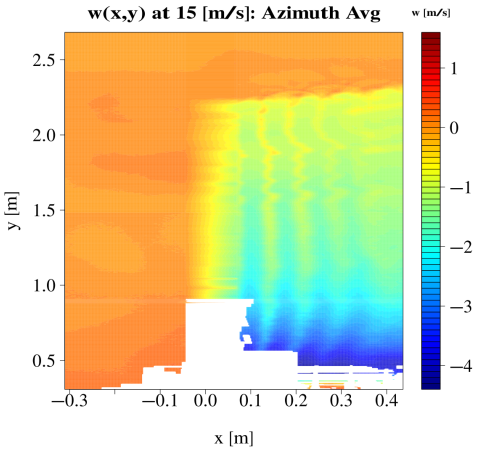

Figure 16. Distribution of tangential velocity (azimuthally averaged) in Radial Traverse at $\lambda = 6.67$

The blade passing period can be reckoned by the cyclic vertical color gradients associated to the viscous wake. Since V_{θ_w} oscillates with the x coordinate, the angular momentum from Equation 12 would fluctuate depending on which position is fixed downstream. Thus, to mitigate this effect, the tangential velocities were averaged within an axial domain embracing 3 passing

wakes, or a full rotor revolution. Only for the $\lambda = 4.16$ case 2 viscous wakes were enveloped owing to null data found near the inboard span. The comparison of blade torque with the angular momentum produced in the wake is shown in Figures 17 - 19.

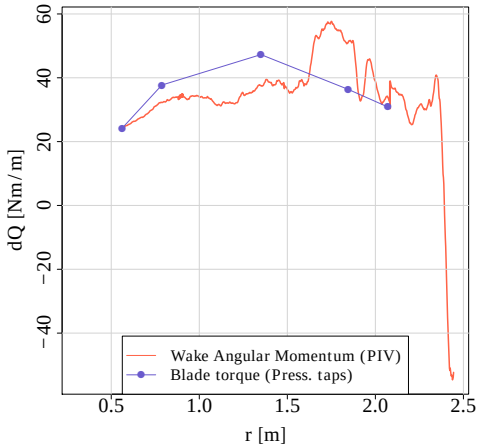

Figure 17. Radial distribution of torque and angular momentum at $\lambda = 9.96$

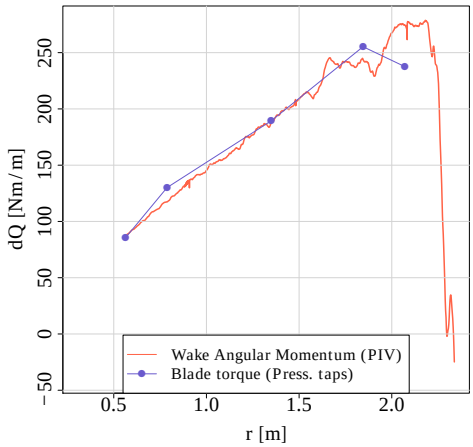

Figure 18. Radial distribution of torque and angular momentum at $\lambda = 6.67$

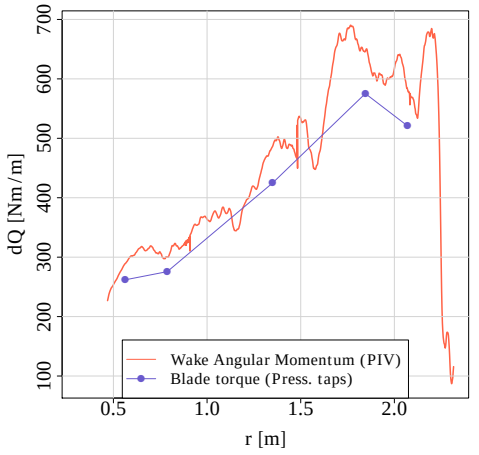

Figure 19. Radial distribution of torque and angular momentum at $\lambda = 4.16$

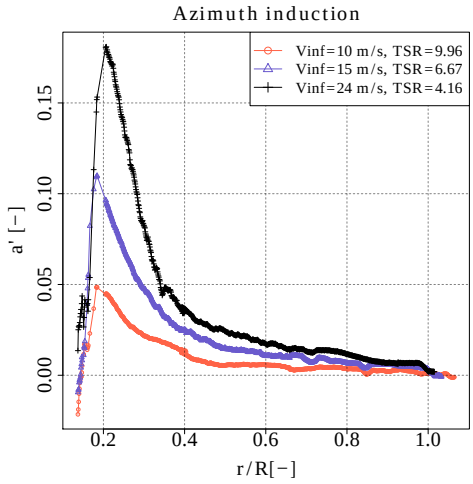

Figure 20. Non-dimensional radius vs. azimuth induction at three λ

There seems to be a reasonable compatibility between the two curves, especially for $\lambda = 9.96$ and 6.67. Some sources of difference can be caused by the viscous effects neglected in the pressure transducers which are well captured in the wake velocities from PIV. On the other hand, the magnitude of azimuth velocities remarkably decrease at high radius. This can be perceived in Figure 20, where the tangential velocities are non-dimensionalized with the rotor frequency Ω and radius r as:

$$a' = \frac{V_{\theta_w}}{2\Omega r} \tag{13}$$

The low azimuth velocities could possibly interfere with the sensitivity of the PIV accuracy, which combined with the mentioned high radius (and in the case of $\lambda = 4.16$ also the high axial velocity) may result in marked variations of the calculated angular momentum (see Equation 12). Additional uncertainty for the last case can be attributed to the presence of flow separation over the blades. Hence the formation and convection of eddies downstream may add for the wake unsteadiness. All in all, it seems that the differences pertain to the scope of each measuring approach. Hence, no apparent correction seems to be needed for the moment of momentum implemented in annular streamtube theory.

5.5. Analytical considerations for the azimuth induction factor

The dependency of a' values with the radius shown in Figure 20 was obtained using directly the azimuth wake velocities behind the rotor. Alternative methods to reconstruct the radial distributions can be investigated based on the works of Glauert [11] and Burton et al. [12] using the local axial velocities and the following initial assumptions: $P_0 = P_1$ and $b = 2a$. By means of energy considerations, Glauert found the pressure drop across the rotor, which multiplied by its area yields an expression to be equated with the change in axial momentum:

$$\underbrace{2\rho V_{x_0}^2 a(1-a)dA_r}_{\text{change in ax. momentum}} = \underbrace{2\rho\Omega^2 r^2 a'(1+a')dA_r}_{\Delta P dA_r} \tag{14}$$

$$a(1-a) = a'\lambda_r^2(1+a') \tag{15}$$

where $\lambda_r = \Omega r/V_{x_0}$ is the local speed ratio. Burton et al. offer an alternative formulation [12]. By equating the rotor power as the torque times the change in angular momentum with the axial force times flow velocity they arrive to the following expression:

$$\underbrace{2\rho V_{x_0} a'(1-a)\Omega^2 r^2 dA_r}_{\text{power from ang. momentum}} = \underbrace{2\rho V_{x_0}^3 a(1-a)^2 dA_r}_{dF_x V_{x_r}} \tag{16}$$

$$a(1-a) = a'\lambda_r^2 \tag{17}$$

Equations 15 and 17, are similar, though Glauert's expression is of higher order. The right hand side of Equation 16 states that the power results only from the contribution of the work developed by the axial force (as in 1D theory) in contrast to a fuller version contemplating the work developed by the torque:

$$dP = dF_{x_r} V_{x_r} - \frac{1}{2}\frac{V_{\theta_r}}{r} dQ \tag{18}$$

where dP is the power at the annulus. If this later expression is replaced, the result from Glauert is in fact recovered. For each approach, the distribution of a' along the radius was solved using the known a values from Figure 9. The comparison for each tip speed ratio is shown in Figures 21 - 23

The curves show negligible differences for r/R values higher than 0.25. Nevertheless, at lower radius more notable discrepancies appear between the three curves. This is to be expected as both formulations, from Glauert and Burton et al., introduce assumptions associated to the pressure deficit influence within the set of equations; an influence that becomes strong towards the root vortex. It is worth noticing, though, that Glauerts method yields results closer to the original curve (in black) for the three cases. Furthermore, the impact of the additional term from Eq. 15 seems to gain significance at lower λ values were the peak values differ more remarkably.

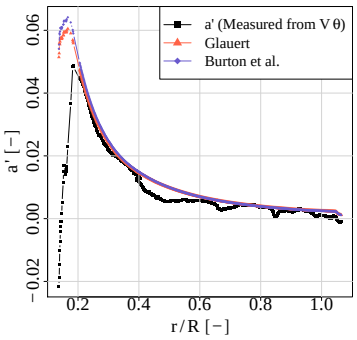

Figure 21. $a'(r)$ at $\lambda = 9.96$. Model comparison

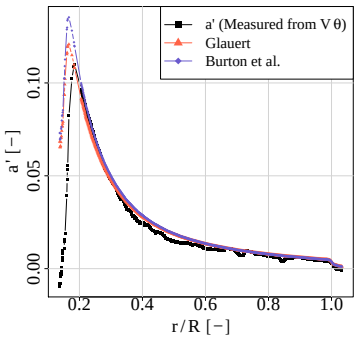

Figure 22. $a'(r)$ at $\lambda = 6.67$. Model comparison

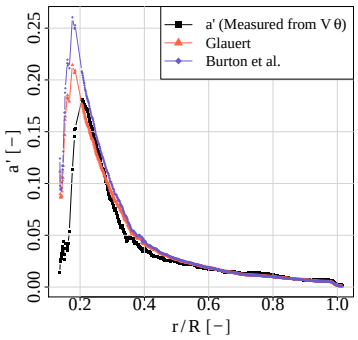

Figure 23. $a'(r)$ at $\lambda = 4.16$. Model comparison

6. Conclusions

The comparison of integral loads with the resultant momentum balance shows an agreement of 0.7% between the pressures on the blades and the global flow field (Figure 4). However, the wake pressure deficit associated to flow rotation complements the radial distribution of velocities as well. Hence both, the change of momentum and pressure surface force were needed to fulfill the integral axial momentum balance.

The classical momentum theory applied at independent annular sections neglects the pressure terms in the momentum equilibrium. The error of this approach seems qualitatively modest and it is to be reflected by scatter of datapoints in Figure 13. The scatter is very low at low inductions with a mean absolute error of 3.9%, but progressively increases to 6.2% at high loading conditions before approaching the turbulent wake state. This hints for a detriment on the validity of this simplification in proportion to the induction or loading state.

The relation between rotor and wake axial velocities $b = 2a$ seems a reasonable approximation for the case studied here. However more details near the root and the tip would be needed to support further evidence.

The angular momentum balance compares well with the sectional torques (Figures 17-19). It is worth noting that even in the turbulent wake state both results seem to match well with each other, which is clearly not the case in axial momentum. Some differences are found for the high wind speed case at $\lambda = 4.16$, although this can be presumably attributed to accuracy aspects in each of the measurements.

Finally, theoretical relations between the axial and azimuth induction factors developed by Glauert and Burton et al. have been evaluated against the measured velocities. It is shown that both models predict the azimuth velocities accurately for most of the blade span above 25% span. The differences are situated near the root vortex, where Glauert's model fits better with the wake measurements.

References

[1] Boorsma K and Schepers J G 2014 *The New MEXICO Experiment: Overview and Preliminary Results* ECN-E14-048, Petten, Netherlands.
[2] Sørensen J N 2016 *General Momentum Theory for Horizontal Axis Wind Turbines* (Springer vol 4) chapter 4
[3] Sharpe D J 2004 *Wind Energy* **7** 177-188
[4] Chen J and Katz J 2005 *Measurement Science and Technology* **16** 1605-1618.
[5] Boorsma K and Schepers J G 2015 *Description of Experimental Setup* ECN-X15-093, Petten, Netherlands.
[6] Sørensen J N and Mikkelsen R 2012 *A critical view on momentum theory.* Presented at the Torque conference series 2012.

[7] Hauptmann S, Bülk M, Schön L, Erbslöh S, Boorsma K, Grasso F, Kühn M and Cheng P W 2014 *J. Phys.: Conf. Ser.* **555**
[8] Schepers J G and Snel H 2007 *MEXICO, Model experiments in controlled conditions* ECN-E-07-042, Petten, Netherlands.
[9] De Vries O 1979 *Fluid Dynamic Aspects of Wind Energy Conversion* AGARD Appendix C.4
[10] van Kuik G A M, Sørensen J N and Okulov V L 1979 *Progress in Aerospace Sciences* **73** pp 10
[11] Glauert H 1935 *Airplane propellers* Springer Berlin Heidelberg
[12] Burton T, Sharpe D, Jenkins N and Bossanyi E 2002 *Wind Energy Handbook* Wiley, pp 41-49
[13] Réthoré P E, Sørensen N N, Zahle F, Bechmann A and Madsen H A 2011 *MEXICO Wind Tunnel and Wind Turbine modelled in CFD.* Applied Aerodynamics Conference. AIAA 2011-3373